Probability-based methods for quantifying nonlinearity in the ENSO

A. Hannachi[1, ✉]**, D. B. Stephenson**[1] **and K. R. Sperber**[2]

(1) Department of Meteorology, the University of Reading, Earley Gate PO Box 243, Reading RG6 6BB, UK

(2) Program for Climate Model Diagnosis and Intercomparison, Lawrence Livermore National Laboratory, P.O. Box 808, L-264 Livermore, CA 94550, USA

✉ E-mail: han@met.rdg.ac.uk

Abstract. Robust statistical tools have been used to investigate non-normality and nonlinearity of the El Niño Southern Oscillation (ENSO) in observations and coupled model simulations. The analysis confirms previous suggestions that the observed Niño-3 sea surface temperature (SST) anomalies are positively skewed. The non-linearity is estimated using a simple nonlinear stochastic model, which relates the sea surface temperature anomalies to the observed thermocline depth anomalies in the Niño-3 region. There is evidence that saturation of SST only occurs when the thermocline is deep. The nonlinearity has also been estimated for the Niño-3 SST indices from twenty four different coupled models participating in the El Niño Simulation Intercomparison Project (ENSIP). Large differences are found between models and observations. In particular, the majority of the coupled models underestimate the nonlinearity seen in the observed Niño-3 sea surface temperature index. More than half of the models have Niño-3 SST indices that are normally distributed at 99% confidence level. Only a few models exhibit significant nonlinearity yet this tends to be rather different in character from the nonlinearity seen in the observations. Furthermore, no significant association is found between the means and the spread nor between the spread and the skewness for the different coupled model Niño-3 SST indices.

1

Introduction

El Niño Southern Oscillation (ENSO), the largest climate phenomenon on the planet, is primarily a coupled ocean-atmosphere phenomenon in the tropical Pacific (Philander *1990*). It can be considered to be a coupled nonlinear oscillator forced by stochastic weather events such as westerly wind bursts (Philander *1990*; Kindle and Phoebus *1995*; Burgers *1999*). It has a large impact on atmospheric circulation through teleconnection from the tropics, which influences the large scale redistribution of vorticity (Bjerknes *1969*, *1972*; Horel and Wallace *1981*; Hoskins and Karoly *1981*; Trenberth et al. *1998* and references therein). For example, the El Niño event of 1982-83 was so strong that the sufficiently strong winds generated through a remarkable atmospheric response slowed down the earth resulting in an increase in the length of the day by about 1/5 of a millisecond

(Salstein and Rosen *1984*). The effect of ENSO on the northern hemispheric circulation is obtained through air-sea interaction, and involves nonlinear processes of thermodynamical control on deep convection by which the midlatitude is likely to respond nonlinearly (Hoerling et al. *1997*; Zhang and Wallace *1996*; Sardeshmukh et al. *2000*; Hannachi *2001*).

A major feature of ENSO is the clear asymmetry between the positive phase, El Niño, and the negative phase, La Niña of the "oscillation" (see Hoerling et al. *1997*; Sardeshmukh et al. *2000*). Table 1 shows the events corresponding to the ten largest magnitude Niño-3 SST anomalies in December over periods of three consecutive years over the last three decades of the record, i.e. from 1971 to 2000. Both the non-detrended and detrended Niño-3 SST anomaly time series are used in Table 1. The detrended time series is obtained by removing a linear trend. Table 1 shows that El Niño events have generally larger magnitudes than La Niña's and that this observation is not affected by the (weak) trend. Note the strong 1997/98 El Niño event, which has been hailed as the El Niño of the century (Wolter and Timlin *1998*). Table 2 shows the number of Niño-3 SST events classified into 0.5 °C wide bins again for both the non-detrended and detrended Niño-3 SST anomalies. Table 2 clearly shows the asymmetry between the number of positive and negative SST anomaly events again irrespective of the trend. The number of positive SST events are larger than their negative counter-parts.

Table 1. The ten largest magnitude Niño-3 SST anomalies (°C) in December over periods of three consecutive years from 1971 to 2000. The anomalies are computed with respect to the annual cycle. The three major El Niño events during this period are in bold. The detrended time series is obtained by removing a linear trend from the Niño-3 SST anomalies

Year	**1972**	1975	1979	**1982**	1984	1988	1991	1994	**1997**	1999
SST (°C)	**2.48**	-1.64	0.46	**3.34**	-1.38	-1.89	1.39	1.01	**3.77**	-1.48
Detrended SST (°C)	**2.50**	-1.64	0.43	**3.29**	-1.45	-1.99	1.27	0.86	**3.60**	-1.66

Table 2. Number of Niño-3 SST anomaly events classified into 0.5 °C wide bins for both the non-detrended and detrended Niño-3 index. For example, in the interval -1.5 °C $\leq$ SST < -1 °C, there are respectively 43 and 42 events in the non-detrended and detrended Niño-3 index in the entire record between 1950 and 2000

Limits (°C)	-3	-2.5	-2	-1.5	-1	-0.5	0	0.5	1	1.5	2	2.5	3	3.5	4
Niño-3 index		0	1	17	43	132	157	115	61	50	17	7	4	6	2
Detrended Niño-3 index		0	0	17	42	131	159	111	65	51	17	8	5	4	2

A natural question arises as to how best can we understand and diagnose such asymmetric behaviour? To answer this question it is necessary to understand the nature of the nonlinearity present in the system. Investigating nonlinearity for a given system is best approached using a probabilistic frame work. The probability distribution function (p.d.f.) of a time series can provide useful information regarding its normal (Gaussian) versus non-normal behaviour. Penland and Sardeshmukh (*1995a*) analysed the 41-year (1950-1990) monthly mean Niño-3 SST anomalies for normality in order to validate their linear system driven by Gaussian white noise. They suggest that SST anomalies deviate equally from Gaussian behaviour during both extreme warm and cold events (see their Fig. 11a), but skewness was not discussed nor any formal statistical test was carried out. Also, in his review on the meaning of the term "El Niño", Trenberth (*1997*) computed histograms of two ENSO indices for the period Jan 1950-Mar 1997, and pointed out in particular that the

Niño-3 index is "strongly" positively skewed (see his Fig. 2) although no formal statistical test was carried out. Burgers and Stephenson (*1999*) showed that the observed Niño-3 SST index was significantly positively skewed. They used moment measures of skewness and kurtosis to assess the non-normal behaviour of various Niño indices. However, these measures are non-resistant and non robust (Lazante *1996*) and can be sensitive to outliers (Hosking *1990*). This study has used more robust and resistant techniques based on quantiles and L-moments (Hosking *1990*) to analyse the observed Niño-3 time series. In addition, these results have been interpreted physically by developing a simple stochastic model that has a nonlinear transfer function.

Because of the importance of the phenomenon, it is important that climate models can correctly simulate ENSO variability. Compared to early climate models, whose simulations of the interannual tropical Pacific SST variability were typically about 50% the observed amplitude (Sperber et al. *1987*; Lau et al. *1992*; Tett *1995*), the recent generation of global coupled models has made significant improvement. While some models simulate realistic amounts of Niño-3 SST variance, many models either under or over estimate variance in the western Pacific, and the annual cycle of tropical Pacific SST is often poorly simulated (Latif et al. *2002*). A major shortcoming is the underestimate of the windstress variance in the western/central tropical Pacific, which is clearly related to the Niño-3 SST variance (Davey et al. *2001*). Additionally, coupled climate models often incorrectly simulate other aspects of ENSO variability, such as the periods of events, and aspects related to nonlinearity. For example, different global coupled models often give shorter ENSO periods of 3-4 years as pointed out by Timmermann et al. (*1999*), AchutaRao et al. (*2002*) and Meehl et al. (*2001*). Burgers and Stephenson (*1999*) also showed that several coupled models were unable to reproduce the observed skewness and kurtosis, and therefore fail to capture correctly the nonlinear aspects of ENSO. In the present study, we have extended this approach by applying more robust techniques to estimate the nonlinearity in the Niño-3 SST time series from 24 coupled models participating in the El Niño Simulation Intercomparison Project (ENSIP, Latif et al. *2002*). The comparison between the observations and model simulations using robust tools provides much needed validations of the models.

The manuscript is organised as follows. In Sect. 2, we briefly review different paradigms underlying ENSO variability, and then introduce a simple nonlinear stochastic model for the Niño-3 SST time series. In Sect. 3, the robust statistical techniques are presented and applied to the observed Niño-3 SST index. An interpretation is presented based on the simple model using observed Niño-3 SST and thermocline depth time series. Estimation of nonlinearity in the model-simulated data is presented in Sect. 4. Conclusions and summary are given in the last section.

2

Conceptual models for ENSO

2.1

Linearity of ENSO

It has been argued that ENSO can be understood as a linear oscillator driven by Gaussian white noise (Graham and White *1988*; Penland and Magorian *1993*; Penland and Sardeshmukh *1995a*, *b*; Wunsch *1999*; Burgers *1999*; Thompson and Battisti *2000*; and references therein). For example, Penland and Sardeshmukh (*1995a*) argued that ENSO may be described as a stable linear dynamical system driven by spatially coherent Gaussian white noise. If this were true ENSO indices should be normally distributed with a similar number of positive (El Niño) and negative (La

Niña) events. However, the observed asymmetry between these number of events (Tables 1, 2) show that this is not the case, see also Trenberth (*1997*) for the positive skewness of Niño-3 SST anomalies. Various Niño-SST indices have been shown by Burgers and Stephenson (*1999*) to be significantly skewed. Thompson and Battisti (*2001*) conducted various experiments with an intermediate coupled model to simulate ENSO. When nonlinearity was included in their experiment they found that the skewness of their ENSO index became positive leading to more frequent warm events than cold events. They concluded that nonlinearity is an important factor particularly in the cold tongue region of the eastern Pacific where it serves to modify the amplitude of ENSO events via horizontal advection and upwelling.

Irregularity in ENSO can arise from either stochastic forcing (weather events) or inherent nonlinearity. Conceptual models for ENSO include the linear stochastic oscillator discussed in the previous paragraph, stochastic nonlinear oscillators (Cane and Zebiak *1985*; Suarez and Schopf *1988*; Munnich et al. *1991*; Neelin et al. *1998* and references therein), or even more exotic fully chaotic systems (Jin et al. *1994*; Stone et al. *1998*). There is still an ongoing debate on whether ENSO should be considered to be a stochastic oscillator or a stable attractor sustained by noise (Neelin *1990*). It is therefore crucial to assess and quantify how much nonlinearity there is in ENSO. This can be achieved by developing nonlinear models to account for the observed skewness.

ENSO is often considered to be dominated by a single oscillating mode that can be explained by the delayed oscillator mechanism (Suarez and Schopf *1988*; Battisti and Hirst *1989*; Kleeman *1993*; Burgers *1999*). A positive SST anomaly in the eastern Pacific can generate westerly wind anomalies in the central equatorial Pacific. These excite eastward propagating Kelvin waves in the equatorial wave guide that deepen the thermocline in the east and enhance eastward transport of warm water from the western warm pool increasing therefore the SST in the eastern Pacific. They also generate westward propagating Rossby waves, which reflect back on the western boundary as delayed Kelvin waves that decrease the SST in the eastern Pacific. Instead of using one SST variable at two time levels, two variables at one level may be taken (Burgers *1999*). A good choice for second variable is the thermocline depth (Jin *1997*; Li *1997*). In this study, a similar approach has been adopted in order to develop a simple stochastic nonlinear model, based on Niño-3 SST and thermocline depth anomalies.

2.2

A simple nonlinear stochastic model

A simple nonlinear model for Niño-3 SST can be written as:

$$Y_t = g(X_t) \tag{1}$$

where Y_t is the Niño-3 SST anomaly and X_t is the thermocline depth anomaly in the Niño-3 region and $g()$ is a monotonic "transfer function". The transfer function $g()$ is most likely monotonic because of the lack of inversions in the vertical profile of large scale monthly mean temperatures. In addition, since the deeper the thermocline the larger the SST anomaly, the transfer function $g()$ is expected to be monotonically increasing. The thermocline depth varies stochastically as normally distributed random variable (see Sect. 3.5). Given the inherent nondeterministic nature of Niño-3 SST, a probabilistic approach is required to address the questions such as nonlinearity. ENSO is intrinsically related to the depth of the thermocline; when the thermocline is shallow any perturbation (due to wind bursts for example) has a strong effect on SSTs. On the other hand a substantial change of the thermocline depth is required to affect the SST when the thermocline is

deep.

When the transfer function is linear, $g(X_t) = \alpha X_t$, the resulting time series Y_t will also be normally distributed. Deviations from normality in Y_t can be used to infer the amount of nonlinearity in the transfer function. Note however that normality of Y_t does not necessarily imply that the transfer function is linear. In the following section, we will present a method for estimating $g()$ using a probabilistic approach.

3

Nonlinearity in the observations

3.1

Observed time series

The Niño-3 SST index is the most widely used measure of ENSO variability (Trenberth *1997*), although other measures such as the multivariate ENSO index (Wolter and Timlin *1998*) are also used. The observed ENSO Niño-3 index used in this study is from the National Center for Environmental Prediction (NCEP) Reanalyses. It is obtained by averaging the sea surface temperature (SST) over the Niño-3 region in the east tropical Pacific between 5°S-5°N and 90°W-150°W (see http://ftp.ncep.noaa.gov/pub/cpc/wd52dg/data/indices/sstoi.indices). The period from 1982 onwards uses the optimal interpolation dataset of Reynolds and Smith (*1994*). Prior to 1982, the Global Sea-Ice and sea surface temperature (GISST) data were used (Rayner et al. *1996*). The sample consists of 612 monthly means from January 1950 to December 2000. We choose to focus on monthly data for two basic reasons: (1) sampling, and (2) importance of the annual cycle in ENSO variability. Figure 1 shows the Niño-3 time series from January 1950 through to December 2000. The apparent regular oscillations in Fig. 1 simply reflect the strong annual cycle that will be discussed in Sect. 3.2.
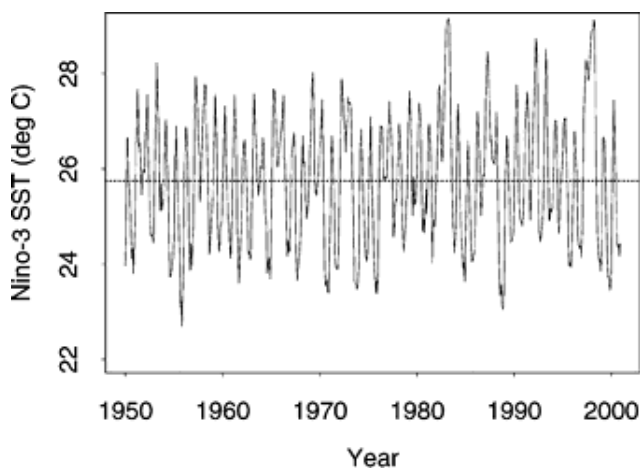
Fig. 1. Time series of the observed Niño-3 SST (°C) from January 1950 to December 2000 obtained by averaging the monthly SST over the Niño-3 region in the tropical east Pacific between 5°N-5°S and 90°W-150°W. The *dotted line* shows the time mean, 25.8 °C

To relate the SST variability in the Niño-3 region to subsurface oceanic characteristics we have created a monthly mean time series of the thermocline depth. The time series of the 20 °C isotherm depth in the Niño-3 region is usually taken as a proxy for the thermocline depth (Meehl et al. *2001*, and references therein.) The thermocline depth data we have used come from moored ocean buoys measurements and are available from the Pacific Marine Environment Laboratory for the Tropical Atmosphere Ocean Project (McPhaden et al. *1998*). Meehl et al. (*2001*) used the depth of the 20 °C isotherm at 155°W on the equator to diagnose the thermocline depth. However, the data contain many missing values particularly around the beginning of the record during the 1980s to the early 1990s. In this study, we prefer to use the station at (0°N, 140°W) which is the nearest one to 155°W, but has the longest record. Other stations also have been used for comparison but are not shown here. Monthly mean values are formed by averaging the daily data of the thermocline depth. Figure 2 shows the time series of the monthly mean depth of the 20 °C isotherm at (0°N, 140°W) from April 1983 to December 2000.
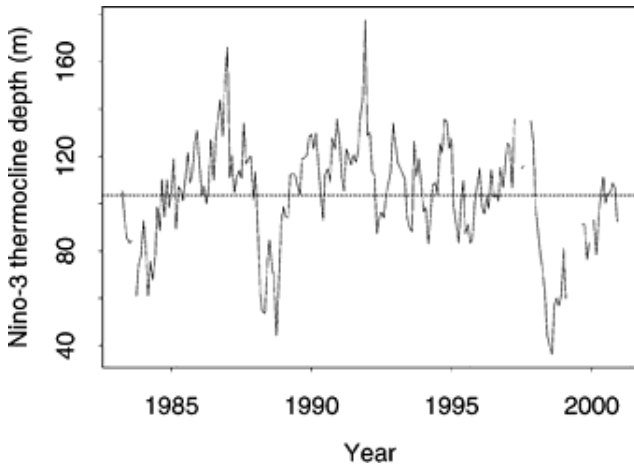
Fig. 2. Monthly time series of the observed 20 °C isotherm depth (m) at (0°N, 140°W) from April 1983 to December 2000

3.2

Empirical distribution function

The cumulative distribution function (c.d.f.) of a random variable Y is defined as:

$$F(y) = Pr\,(Y \leq y) = \int_{-\infty}^{y} f(u)\mathrm{d}u \tag{2}$$

where $Pr()$ is the "probability of" and $f()$ is the probability density function (p.d.f.) of Y. To obtain an "empirical" estimate of the cumulative distribution function from an observed time series we simply use $F(y_i) = (rank(y_i) - 1)/(n - 1)$ where $rank(y_i)$ is the position of y_i once all the y_i are arranged in ascending order. Various ways exist for smoothing the c.d.f. estimate but these are not addressed here (see e.g. Silverman *1994*). The value $y_p = F^{-1}(p)$ corresponding to a specified probability value $0 \leq p \leq 1$ is known as the p'th "quantile"; for example, the median is the

quantile $y_{0.5} = F^{-1}(0.5)$.

Quantiles are robust ways of summarizing distributions. A widely used powerful graphical technique for summarizing data is the "boxplot". It is a graphical representation showing the centre, the spread and the skewness of a distribution along with a display of unusually deviant data points or outliers. Boxplots (McGill et al. *1978*; Tukey *1990*) have proven to be a good exploratory tool, particularly when several boxplots are plotted side by side for comparison between distributions of different datasets. Figure 3 shows the boxplots corresponding to the different months in the observed Niño-3 SST time series. The central line in the box shows the median $y_{0.5}$. The top and bottom of the box show the upper and lower quartiles, $y_{0.75}$ and $y_{0.25}$, respectively. The height of the box represents the inter-quartile range (IQR) defined as the difference between the third and first quartiles, IQR = $y_{0.75}$ - $y_{0.25}$. The IQR is a robust scale parameter that measures the spread of the data (Lazante *1996*). The whiskers are drawn to the nearest value not beyond a standard span (1.5 × IQR) from the quartiles and they extend to the min(1.5 × IQR, extreme values). The points beyond the whiskers, or outliers, are drawn individually (Fig. 3). Note that for a normal distribution with variance σ^2 the IQR is 1.349 × σ and that the whiskers contain 99.3% of the data.
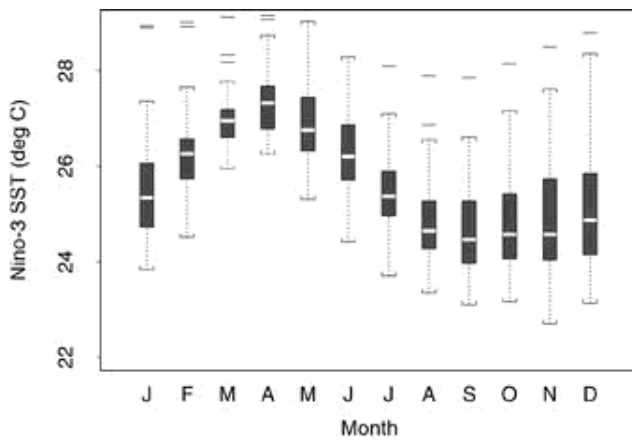

Fig. 3. Boxplots for each month of the observed Niño-3 SST time series. The *height* of the *grey boxes* indicate the IQR whereas the *line* inside each box shows the median. The *whiskers* extend to min(1.5 × IQR, extreme values). *Points* beyond the the whiskers, outliers, are drawn individually

Several outstanding features can be inferred from the boxplots in Fig. 3. The annual cycle of the median is clearly visible. Other common features can also be noted; for example, the interannual spread is strongest during November and December and weakest during March and April (see also Latif et al. *2002*). Note also that February, March, June and July show less pronounced skewness compared to the remaining months. All months except May and June exhibit outlier values particularly in winter/spring.

The observed Niño-3 SST time series can be deseasonalised by removing the annual cycle of the median (Fig. 3). The deseasonalised Niño-3 index is shown in Fig. 4 and has been used in all the following analyses. The histogram and a smooth kernel estimate (Silverman *1994*) of the probability density of all the months of the Niño-3 index are shown in Fig. 5. The dotted line in Fig. 5 shows the normal distribution with the same mean and variance as the observed index. It can

be seen that the distribution of the deseasonalised Niño-3 index is positively skewed as noted in Trenberth (*1997*) and Burgers and Stephenson (*1999*). The asymmetry between the frequency of positive (El Niño) and negative (La Niña), as shown in Tables 1 and 2, is visible in Fig. 5
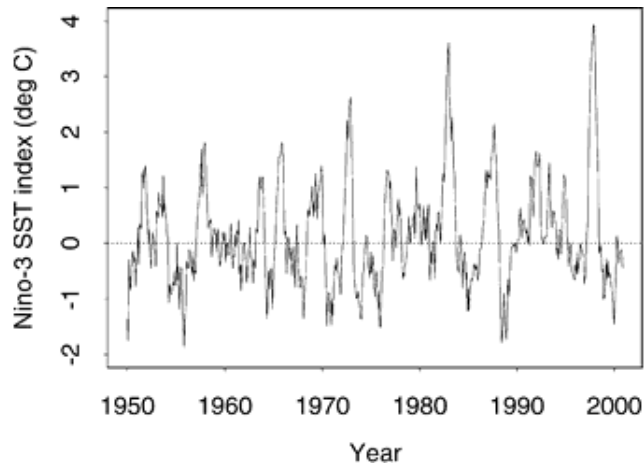
Fig. 4. Deseasonalised Niño-3 SST time series, the Niño-3 index (°C), obtained by removing the annual cycle (median for each month) from the observed time series
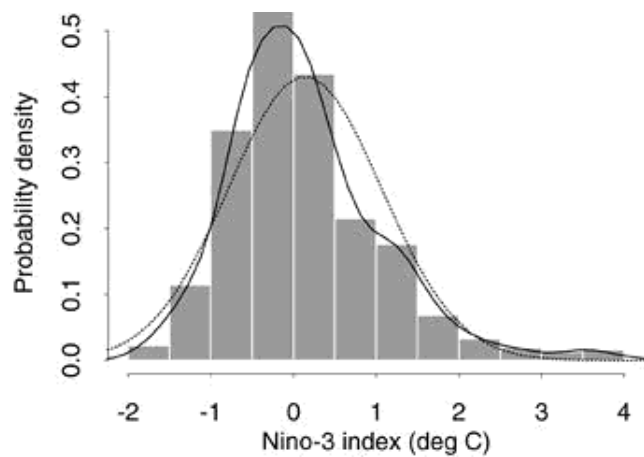
Fig. 5. The histogram (*bars*) and the probability distribution function (*solid line*) of the observed Niño-3 index. The *dotted line* shows the normal distribution with the same mean and variance as the observed index

3.3

Estimating the transfer function

In the case of monthly mean temperatures, where there are unlikely to be any temperature inversions, the monotonic transfer function $g()$ can be estimated by comparing the quantiles of the SSTs with those of the thermocline depth. For a monotonically increasing transfer function $y = g(x)$, the probability p of an SST Y being less than or equal to a value $y_p = g(x_p)$ is equal to the

probability of the thermocline depth X being less than or equal to a value x_p:

$$Pr\left(Y \leq y_p = g(x_p)\right) = Pr\left(X \leq x_p\right) = p \tag{3}$$

where $x_p = F_X^{-1}(p)$ and $y_p = F_Y^{-1}(p)$ are the quantiles of the thermocline depth and the SST, respectively. Therefore,

$$F_Y^{-1}(p) = g(F_X^{-1}(p)) \tag{4}$$

and so the transfer function can easily be found by plotting the quantiles of Y (the SST) versus the quantiles of X (the thermocline depth), that is the quantile-quantile (qq) plot. When only SST data is available, the quantiles of the thermocline depth x_p can be obtained by making an assumption about the probability distribution of thermocline depth. The most reasonable assumption justified by the short record of observed data is that the thermocline depth is normally distributed (see Sect. 3.5). Therefore, $F_X() = \Phi()$, where $\Phi()$ is the area under the standard normal curve, that is the c.d.f. of the standard normal distribution, and the quantiles x_p of the standardised thermocline depth are simply the quantiles of the standard normal distribution, for example, $x_{0.975} = 1.96$.

Figure 6 shows the quantile-quantile plot between the observed Niño-3 index and the standard normal, indicated by a solid curve. If the Niño-3 index were normally distributed the curve would be identical to the diagonal line $y = x$. Deviations from this line indicate the presence of non-normality, and therefore nonlinearity in the transfer function. Figure 6 shows clear deviations from normality which are assessed in Sect. 3.4 using robust L-moments. Possible physical explanations are given in Sect. 3.5. Figure 6 is similar to Fig. 11a of Penland and Sardeshmukh (*1995a*) except that their figure represents a c.d.f. plot in a Gaussian stretched coordinates and not quantiles.
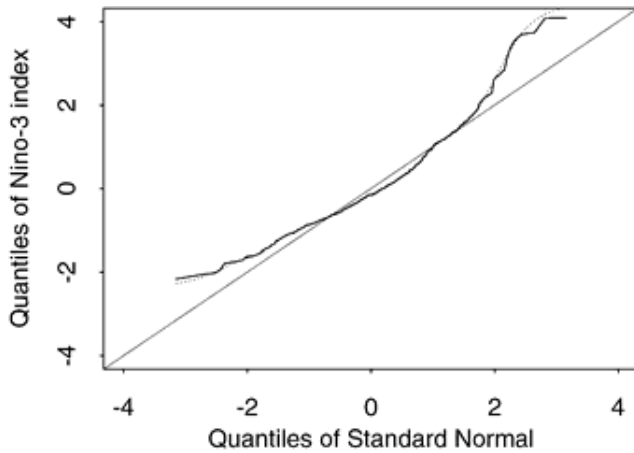
Fig. 6. The quantiles of the standardised observed Niño-3 index versus the quantiles of the standard normal (*bold curve*). The first diagonal represents the curve expected from the standard normal distribution. The departure of the right (*left*) end of the curve above the *first diagonal line* indicates positive skewness or fatter (thinner) tail than the normal. The *dotted curve* is obtained when the quantiles are derived from Eq. (6)

Whereas skewness can often be difficult to see in histograms (Fig. 5), it is clearly visible in quantile-quantile plots (Fig. 6). Positive skewness is reflected by the presence of a deviation of the right side of the curve above the diagonal line. To see this consider any probability p with corresponding quantiles y_p and x_p from the c.d.f.'s F and Φ of the data (SST here) and the standard normal distribution respectively (see Eqs. 3-4). Because the p.d.f. of Y is positively skewed one expects that for large z, $\Phi(z) \geq F(z)$. Therefore, since $\Phi(x_p) = F(y_p)$ (= p), the quantiles satisfy $x_p = \Phi^{-1}(p) \leq y_p = F^{-1}(p)$. The left side of the curve in Fig. 6 is also above the diagonal line but indicates this time a thinner tail than the normal distribution. Positive skewness leads to convex qq-plot curves. A negatively skewed distribution produces a concave qq-plot curve.

3.4

Robust measures of moments

Various quantitative measures can be used to quantify departures from normality (Mardia *1980*). The most commonly used measures are the moment estimates of skewness, b_1, and kurtosis b_2:

$$
\begin{aligned}
b_1 &= m_3/m_2^{3/2} \\
b_2 &= m_4/m_2^2
\end{aligned}
\tag{5}
$$

where m_r is the r'th sample moment about the mean, $E((Y - \bar{Y})^r)$. Note that for the normal distribution $b_1 = 0$ and $b_2 = 3$. The skewness parameter gives a measure of the asymmetry of the probability distribution about the mean whereas the kurtosis parameter gives a measure of the flattening. A negative (positive) skewness gives a p.d.f that is skewed to the left (right). When $b_2 > 3$ the p.d.f. is tall and slim at the centre (leptokurtic), and when $b_2 < 3$ it is platykurtic. Moment measures of skewness and kurtosis, however, are "non-resistant" statistics that are overly sensitive to outliers. Furthermore, it is often difficult to assess exactly what information about the shape of a distribution is conveyed by its third and higher order moments particularly when the sample is small (Hosking *1990*). For example, when the sample is small convergence problems of the sample moments towards the population moments may arise. Furthermore, when the sample contain few outliers, the higher order moments will be controlled by these outliers. More robust and resistant approaches, such as L-moments, have been developed based on order statistics (Hosking *1990* and references therein, see also von Storch and Zwiers *1999* for a brief description).

The quantile $y_p = F^{-1}(p)$ can be expanded as a series of shifted Legendre polynomials as

$$
y_p = \sum_{r=1}^{\infty} (2r - 1)\lambda_r P_{r-1}^*(p) \ .
\tag{6}
$$

The expansion coefficients, λ_r, are known as "L-moments" and are defined as

$$
\lambda_r = \int_0^1 y_p P_{r-1}^*(p) \mathrm{d}p
\tag{7}
$$

where $P_r^*()$ is the r'th shifted Legendre polynomial. Refer to the Appendix for details and for the definition of these polynomials. Any distribution is uniquely specified by its L-moments even if some of its conventional moments do not exist (see Hosking *1990* for details). The lowest order L-moment, λ_1, is simply the mean of the random variable. The second order moment, λ_2, is a robust measure of the spread which uses information from all the quantiles (unlike the IQR). L-moments ratios can be obtained by standardising the L-moments by the scale parameter:

$$\tau_r = \lambda_r/\lambda_2, \quad r = 3, 4, \dots \tag{8}$$

The ratios τ_3 and τ_4 can be regarded as measure of skewness and kurtosis respectively. Note that for the normal distribution $\tau_3 = 0$, and $\tau_4 = 0.1226$.

Figure 7 shows the cumulative distribution function, $F(y_p)$ for the Niño-3 index (solid line) calculated using the expansion Eq. (6) keeping the first 18 terms. The dotted line is the cumulative distribution function expected for the normal distribution with the same mean and variance as the Niño-3 index. Note that the maximum slope of the cumulative distribution gives a measure of the spread. The difference between the two slopes of the cumulative distribution functions at the origin (Fig. 7) is due to skewness in the observed index. The qq-plot of the Niño-3 index using the truncated expansion is shown as a dotted line in the qq-plot of Fig. 6. Note how the thinner (than the normal) tail is even more clearly pronounced with the L-moment approach. The (positive) skewness is made slightly larger with the L-moment quantiles. The dotted curve is also slightly smoother than the solid line.
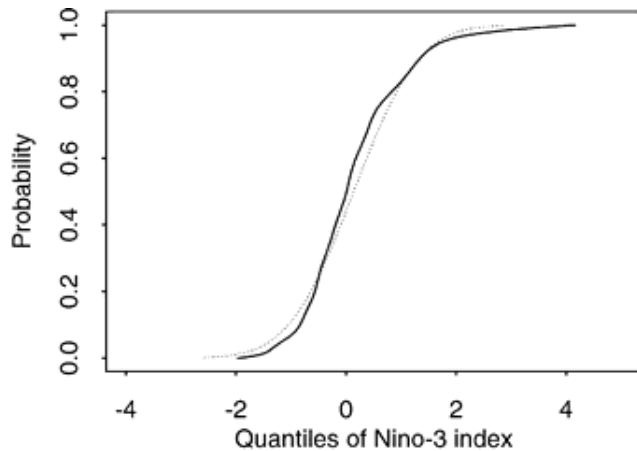
Fig. 7. The cumulative distribution function of the Niño-3 index obtained by using the quantiles from Eq. (6) and keeping the first 18 terms (*solid line*) and the normal with the same mean and variance (*dotted line*)

3.5

Stochastic model validation

Section 3.4 outlined the use of the qq-plot as a simple graphical way to see the relationship between two variables. Here we use this tool to diagnose the non-linear transfer function $g()$ of Eq. (1)
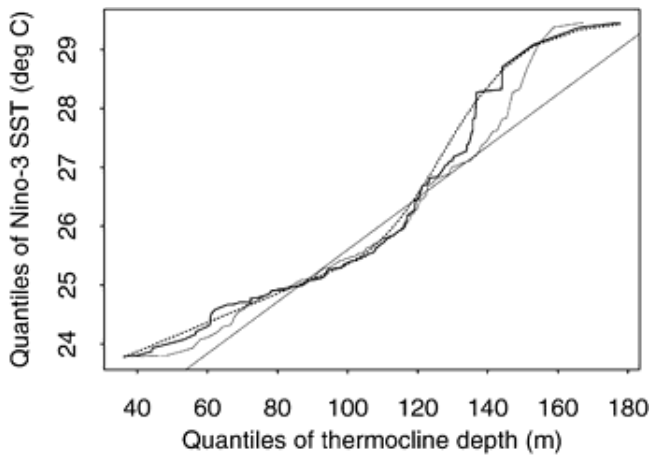
between the Niño-3 SST and the thermocline depth. As a first step in validating the stochastic model, presented in Sect. 2.2, Fig. 8 shows quantiles of the thermocline depth in the Niño-3 region versus quantiles of the standard normal distribution. It indicates that, unlike sea surface temperature anomalies, Niño-3 thermocline depth anomalies do not depart significantly from normality. A Kolmogorov-Smirnov (K-S) test indicates that the time series is normally distributed at more than 95% confidence level. The annual cycle was removed prior to computing the qq-plot (Fig. 8). We found that the seasonality is not a strong modulator of the evolution of the thermocline depth south of 2°N in the east tropical Pacific. However, for the stations on the 5°N latitude in the same region we found a strong seasonal component in the evolution of the thermocline depth. These observations are in agreement with the general feature of a stronger ITCZ north of the equator where the ITCZ annual cycle is well marked in the 5-10°N latitudinal band in the eastern equatorial Pacific (Xie and Arkin 1995; Meehl et al. *2001*).
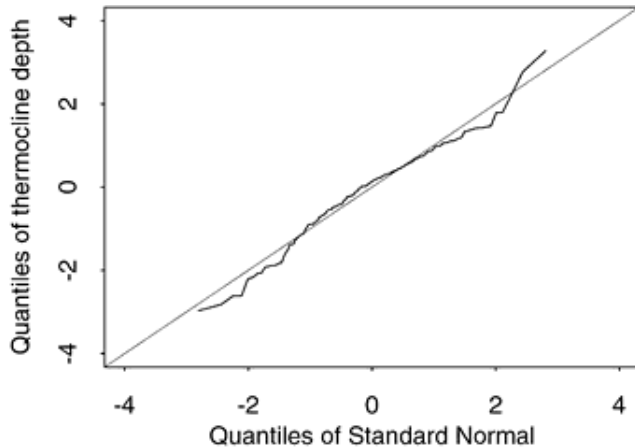
Fig. 8. The quantiles of the standardised 20 °C isotherm depth at (0°N, 140°W) versus the quantiles of the standard normal

---

The quantiles of the Niño-3 SST versus the quantiles of the thermocline depth time series is shown as a thick solid line in Fig. 9. The thin line shows the quantiles of the Niño-3 SST versus the quantiles of the normal distribution with the same mean and standard deviation as the Niño-3 thermocline depth (similar to the solid line in Fig. 6). Note that the Niño-3 SST used in Fig. 9 is obtained by adding the Niño-3 SST climatology to the Niño-3 index. Note the good agreement between both the nonlinear curves. Another feature of this nonlinearity can be noted from the levelling off of the (solid) curve in the top right corner of the panel. This corresponds to a deep thermocline where a large change in thermocline depth induces only small changes in the SST. This saturation starts when the (absolute) thermocline is approximately around 140 m deep, where the SST becomes nearly independent of the thermocline as it deepens. When the thermocline is deep, stratification acts as a barrier between the surface and the thermocline and the link between them becomes very weak.

Fig. 9. The quantiles of the Niño-3 SST index (°C) versus the quantiles of the Niño-3 thermocline depth (m) (*thick line*) and the quantiles of the Niño-3 SST index versus those of the normal distribution with the same mean and standard deviation as the Niño-3 thermocline depth (*thin line*). The *dotted line* shows a smooth fitting to the quantile-quantile curve between the SST and thermocline depth time series. The *first diagonal* is shown for comparison. Note that the Niño-3 time series has been trimmed so that both time series correspond to the same period

It is also interesting to note that the SST changes are most sensitive for thermocline depths between 120 and 140 m with a rate of change around 1 °C per 8 m. For depths less than 120 m, the rate is around 1 °C per 25 m and the lower part of the curve does not saturate at least as sharply as the upper part. Although the 20 °C isotherm does not reach the surface (Fig. 1), it remains in constant contact with the mixed layer when the thermocline is shallow. In this case a slight change in the thermocline depth will not change the SST substantially. This makes the SST-thermocline depth sensitivity fairly linear because of the active mixing processes in the mixed layer and the absence of any barrier such as stratification when the thermocline is shallow (less than a 120 m deep). This explains the observed weaker rate of change of 1 °C per 25 m as opposed to the higher rate observed for depths between 120 m and 140 m. The dotted line in Fig. 9 shows a smooth piecewise fit to the SST-thermocline depth curve (thick line) obtained by fitting a tangent hyperbolic function to the upper half and a straight line fitted to the lower half. Both Zebiak and Cane (1987) and Battisti (*1988*) used a tangent hyperbolic fit over the whole range to parametrise the subsurface temperature anomaly. The tangent hyperbolic parametrisation is unable to capture the behaviour of the transfer function over the whole range. It saturates at both deep and shallow thermocline depths whereas the observations show no evidence of saturation at shallow depths.

4

Nonlinearity in the coupled model simulations

4.1

Model data

Twenty four coupled ocean-atmosphere models from ENSIP have been studied in this investigation. A brief summary of the models is presented in Table 3. The models span a wide-range of parameter space, having been developed for widely varying applications. Many of the global models have

been developed to investigate the anthropogenic climate change, while the Pacific basin models, which tend to employ higher meridional resolution in the ocean, are more directed at process studies related to ENSO. The model data are taken from control integrations (e.g. no anthropogenic forcing). More detailed description of the different models and references can be found in Latif et al. (*2002*) and Davey et al. (*2001*). Some of the models also participated in the coupled model intercomparison project (see http://www-pcmdi.llnl.gov/modeldoc/cmip CMIP, Meehl et al. *2000*). Figure 10 shows the Niño-3 SST time series from each model. The time mean of the observed Niño-3 SST time series is also indicated by a dotted line for comparison. Some summary statistics for the different Niño-3 time series are given in Table 4. The difference between the observed and simulated time means varies considerably. The largest difference is 3.5 °C and is obtained with the DKRZ-LSG model (Fig. 10f) whereas the smallest difference is of the order of 0.05 °C and is obtained with the NCEP climate model (Fig. 10t). Much of the variability in model simulations (Fig. 10) is due to the annual cycle which is briefly analysed in the following section.

Table 3. Some characteristics of the different ENSIP models. In the last column, *P-E* refers to mean flux correction for fresh water

Model	Atmospheric resolution	Ocean resolution	Coupling	Flux adjustment
	lat, lon $\times$ vert	lat $\times$ lon $\times$ vert		
BMRC	R21, L9	0.5-5.9, 2, L25	Global	None
CCC	T32, L10	1.8, 1.8, L29	Global	Heat/*P-E*
CCSR	T21, L20	0.5-2, 2.5, L20	Global	SST relax 55N-90N
CERFACS	T42, L31	0.33-1.5, 0.75, L28	Tropical Pacific	None
COLA	T30, L18	1-3, 3, L20	Global	None
DKRZ-LSG	T21, L19	4, 4, L11	Global	Heat/*P-E*/momentum
DKRZ	T42, L19	0.5-2.8, 2.8, L11	Global	Heat/*P-E*
GFDL-R15	R15, L9	4.5, 3.7, L12	Global	Heat/*P-E*
GFDL-R30	R30, L14	2.24, 1.88, L18	Global	Heat/*P-E*
HAWAII	1, 2, L2	1, 2, L2	Tropical Pacific	Prescribed cloud
JMA	T42, L21	0.5-2, 2.5, L20	Global	None
LAMONT	2, 5.625, 1 mode	0.5, 2, L2	Tropical Pacific	Anomaly coupling
LMD	50 points $\times$ 5.6, L11	0.33-1.5, 0.75, L20	Tropical Pacific	None
LMD-GLOBAL	72 points $\times$ 3.75, L15	0.5-1.5, 2, L31	Global	None
LMD-TOGA	50 points $\times$ 5.625, L11	0.33-1.5, 0.75, L28	Tropical Pacific	None

MPI	T42, L19	0.5-2.8, 2.8, L20	Global	None
MRI	4, 5, L15	0.5-2, 2.5, L21	Global	Heat/*P-E*
NCAR-CSM	T42, L18	1.2, 2.4, L45	Global	None
NCAR-WM	R15, L9	1, 1, L20	Global	None
NCEP	T42, L18	0.33-1, 1.5, L28	Tropical Paccific	1-way/anomaly coupling
NRL	T39, L12	0.5-2, 2, L25	Tropical Paccific	None
SACLAY	50 points × 5.6, L11	1-13, 4, L31	Global	None
UCLA	4, 5, L15	0.33-3, 1, L27	Tropical Pacific	None
UKMO	3.75, 2.5, L19	1.25, 1.25, L20	Global	None
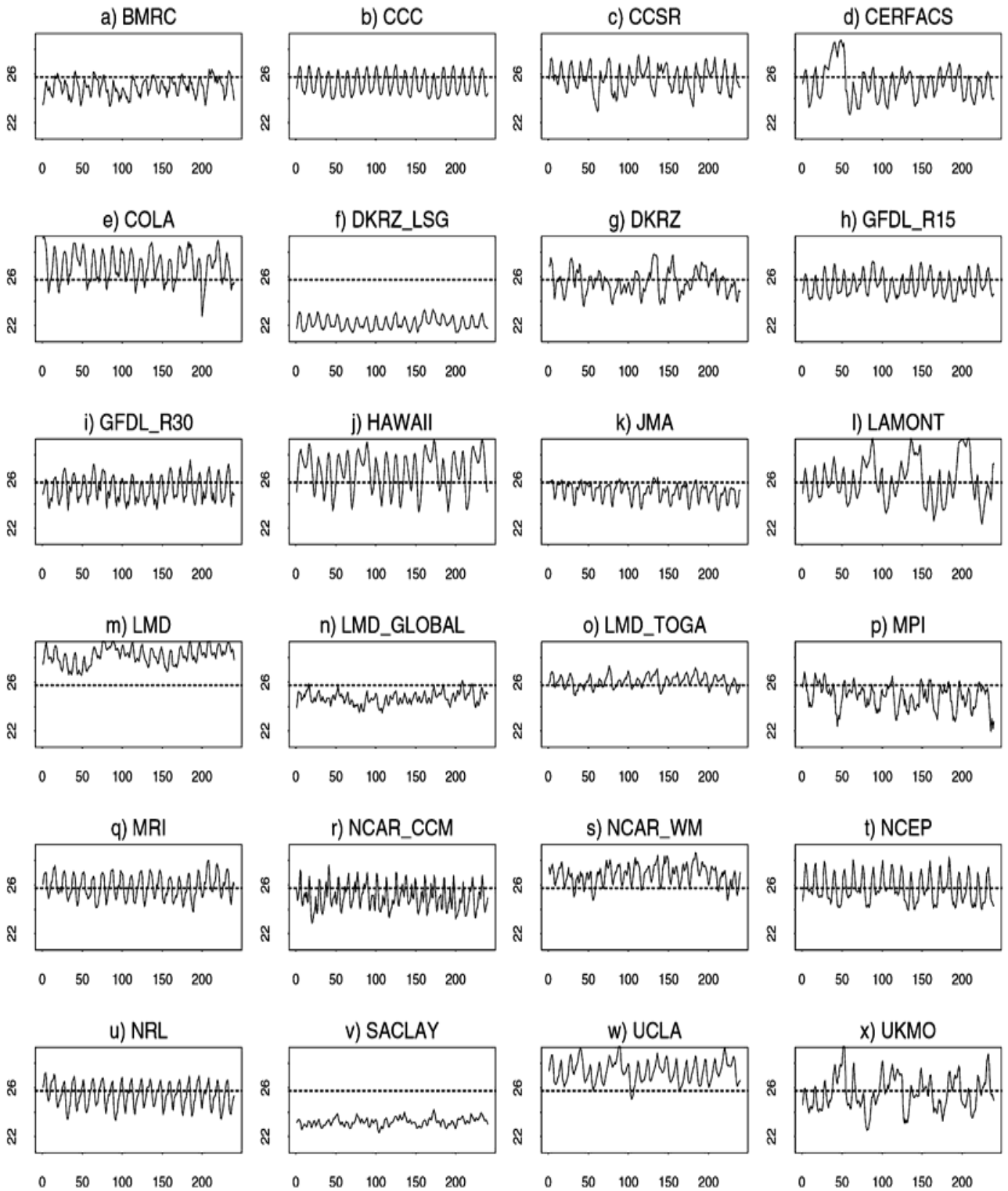
Fig. 10. Time series of the Niño-3 indices (°C) taken from a control run of 24 different coupled models from ENSIP. The *dotted line* in each panel indicates the time mean of the observed index (Fig. 1). The abscissa is time in years

Table 4. A summary of the observed and coupled models statistics of the Niño-3 time series.

Shown are the climatology, standard deviation (S), inter-quartile range (IQR), skewness (b_1), kurtosis (b_2 - 3), and the L-moment ratios τ_3 and τ_4. The P-values when using a Kolmogorov-Smirnov test are also shown. Some of the most non-normal models at 99% confidence are marked by stars

Models and observations	Mean (°C)	S (°C)	IQR (°C)	Skewness b_1	Kurtosis b_2 - 3	τ_3	τ_4	P-value
BMRC	24.9	0.46	0.64	0.23	0.25	0.02	0.14	>0.1
CCC	25.3	0.22	0.29	0.05	0.14	0	0.13	>0.1
CCSR*	25.2	0.81	0.95	-0.47	1.05	-0.05	0.17	0.003
CERFACS*	25.3	1.07	0.95	1.68	3.49	0.26	0.26	0.000
COLA	26.8	0.72	0.83	0.13	1.13	0.05	0.17	0.033
DKRZ-LSG*	22.2	0.22	0.30	0.49	-0.27	0.10	0.11	0.004
DKRZ*	25.6	0.82	1.10	0.59	0.04	0.13	0.11	0.006
GFDL-R15	25.3	0.37	0.50	0.24	0.05	0.04	0.12	0.009
GFDL-R30	25.3	0.40	0.59	0.09	-0.16	0.02	0.11	>0.1
HAWAII	26.7	0.99	1.02	0.26	0.65	0.06	0.21	0.000
JMA	25.0	0.36	0.46	0.06	-0.01	0	0.14	>0.1
LAMONT*	26.0	1.41	2.03	0.60	-0.32	0.14	0.09	0.000
LMD	28.2	0.52	0.64	-0.45	-0.22	-0.11	0.13	0.000
LMD-GLOBAL	24.8	0.40	0.54	-0.28	0.02	-0.03	0.13	>0.1
LMD-TOGA	26.1	0.31	0.45	-0.05	-0.55	-0.01	0.09	>0.1
MPI	24.8	0.80	1.06	-0.27	-0.25	-0.05	0.12	>0.1
MRI	25.9	0.40	0.52	-0.01	-0.21	0	0.13	>0.1
NCAR-CSM	25.0	0.48	0.71	0.06	-0.14	0.01	0.11	>0.1
NCAR-WM	26.8	0.50	0.69	-0.15	-0.23	-0.03	0.13	>0.1
NCEP	25.8	0.44	0.65	-0.19	-0.48	-0.05	0.10	0.000
NRL*	25.4	0.34	0.37	0.31	0.98	0.04	0.20	0.008
SACLAY	23.2	0.27	0.40	0.32	-0.53	0.08	0.08	0.033
UCLA*	27.4	0.57	0.70	0.43	-0.08	0.12	0.14	0.000
UKMO	25.6	1.14	1.54	0.27	-0.33	0.05	0.11	>0.1
Observations*	25.8	0.93	1.05	1.01	1.77	0.16	0.17	0.000

4.2

Annual cycle

Figure 11 shows boxplots of the monthly means for each calendar month for all the different models. There are clear discrepancies between the different coupled models in simulating the

annual cycle. For example, the annual cycle has a very small amplitude in some models such as LMD (Fig. 11m, n, o) and SACLAY (Fig. 11v), and it is also underestimated in BMRC (Fig. 11a), DKRZ-LSG (Fig. 11f), JMA (Fig. 11k), NCAR-WM (Fig. 11s), and UCLA (Fig. 11w). Some models do not simulate correctly the phase of the annual cycle such as, JMA (Fig. 11k), LMD (Fig. 11m, n), SACLAY (Fig. 11r), NCAR-WM (Fig. 11s), MPI (Fig. 11p). For example, Fig. 11m, n, r, s indicate a strong semi-annual-like cycle. The LAMONT and UKMO models (Fig. 11l, x) simulate reasonably well the phase and amplitude of the annual cycle. However, the spread is overly uniform throughout the year compared to that in Fig. 3. Some models, such as CCSR (Fig. 11c), COLA (Fig. 11e), and MPI (Fig. 11p), have negative skewness with negative outlier values that are not seen in the observed SST (Fig. 3).
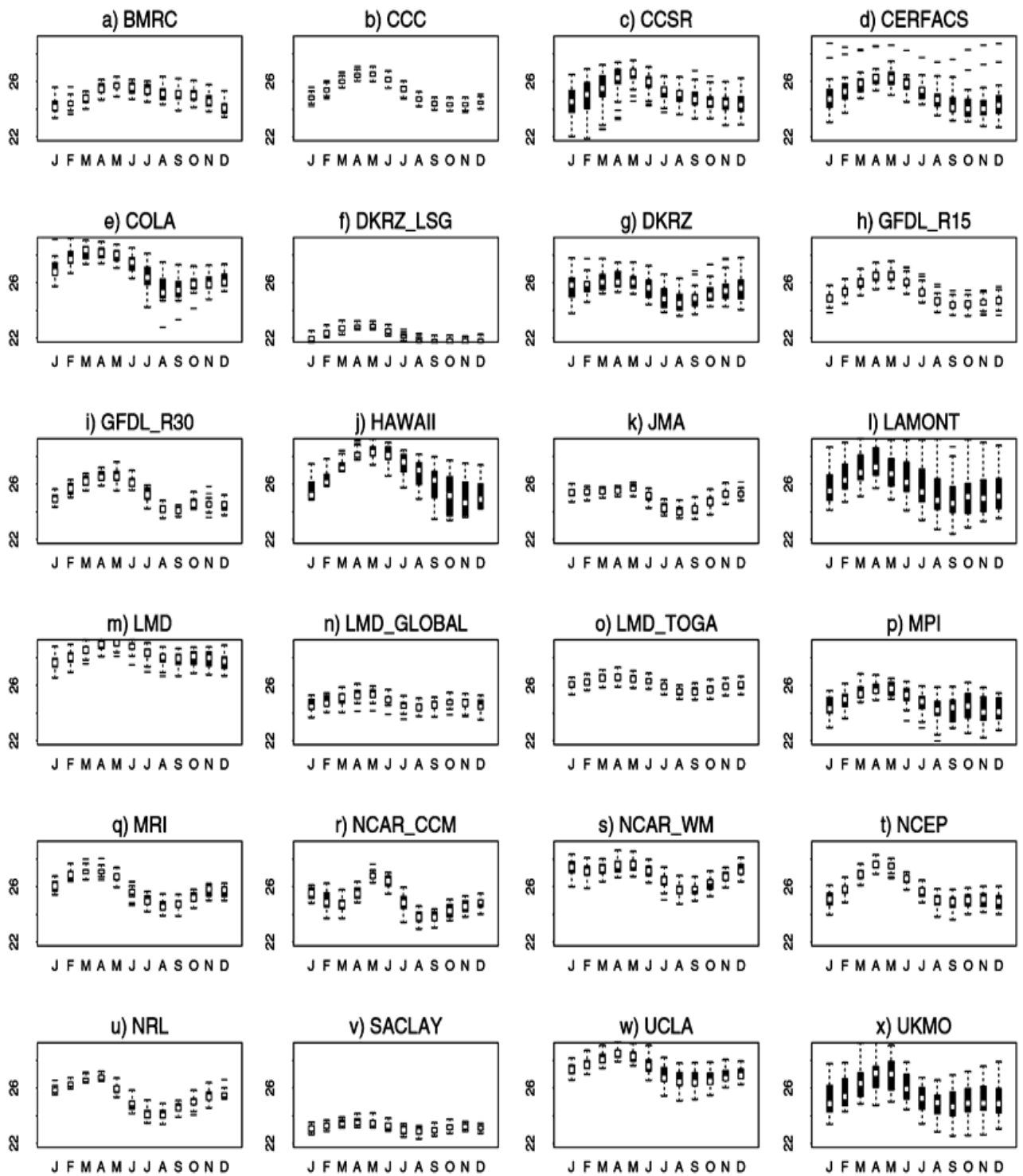
Fig. 11. Boxplots of Niño-3 indices (°C) for each month from the different ENSIP coupled-models. (see Fig. 3)

It is well known that several climate models tend to produce semi-annual cycles of the SST in the eastern tropical Pacific (Mechoso et al. *1995*). Latif et al. (*2002*) find that even flux-corrected models have difficulties simulating a realistic annual cycle.

4.3

Is there nonlinearity in simulated Niño-3 anomalies?

In order to evaluate the interannual variability, the model time series have been deseasonalised by removing the monthly medians. The resulting Niño-3 indices are plotted in Fig. 12. Several models underestimate the variance (e.g. CCC Fig. 12b, DKRZ-LSG Fig. 12f, JMA Fig. 12k, LMD Fig. 12m, n, o, MRI Fig. 12q, SACLAY Fig. 12v), whereas other models overestimate the variance (e.g. CERFACS Fig. 12d, HAWAII Fig. 12j, LAMONT Fig. 12l, UKMO Fig. 12x). The variances of the different Niño-3 indices are shown in column 3 of Table 4. The HAWAII and LAMONT models show smoother than observed variability with less high frequency contribution.
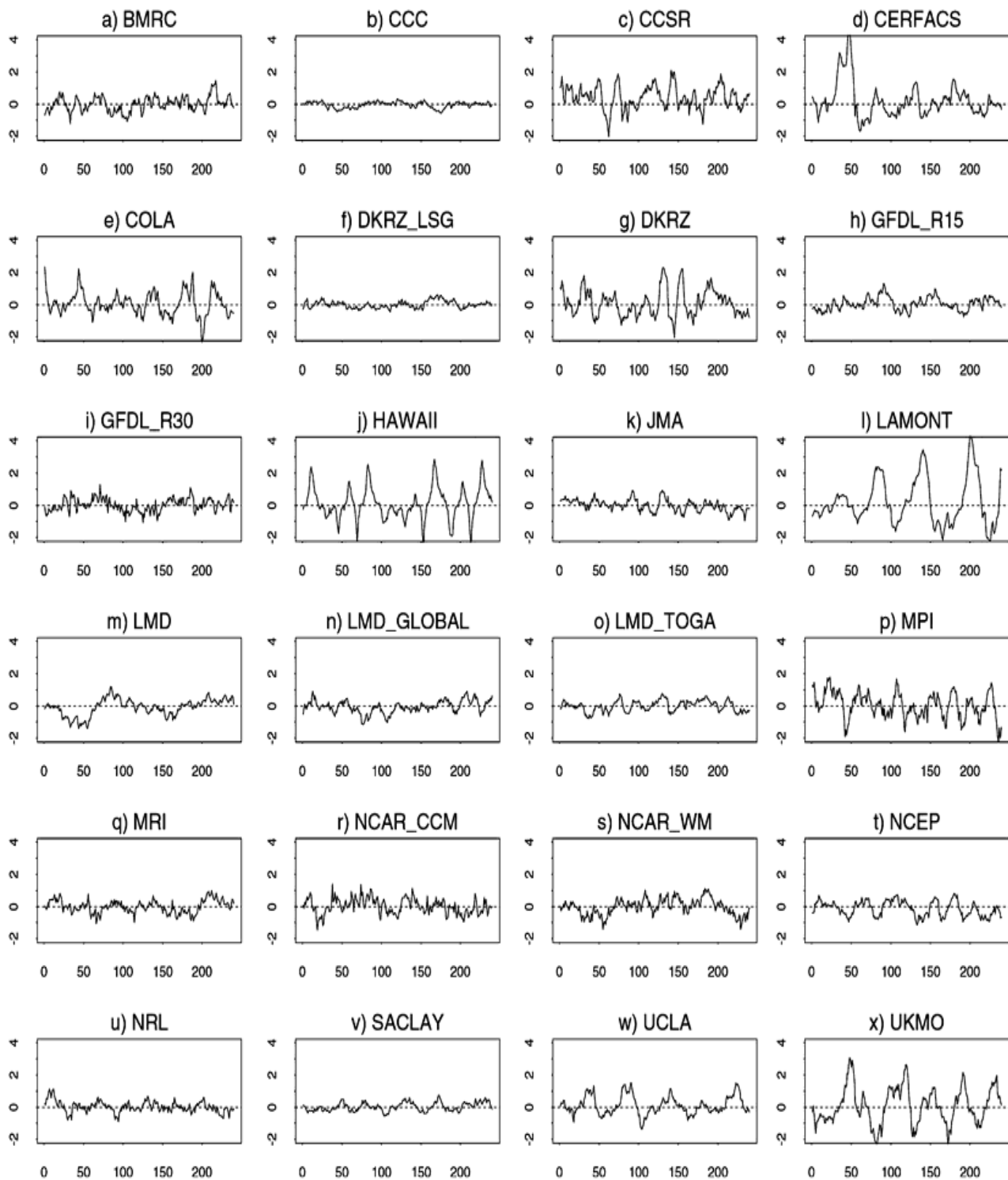
Fig. 12. The deseasonalised Niño-3 indices (°C) from the coupled models. The abscissa is time in years

Figure 13 shows the histograms and the kernel estimates of the probability density functions (solid lines) of the models Niño-3 SST indices. Because of the wide range of variance in the different time series it was not useful to have the same scale on the vertical axes and so each plot has its own

vertical scale. The normal distribution with the same mean and variance for each index is also shown by dotted line. Note in particular the wide range of spreads for the different models. For example, models like CCC (Fig. 13b), DKRZ-LSG (Fig. 13f), GFDL (Fig. 13h, i), JMA (Fig. 13k), LMD(Fig. 13m, n, o), MRI (Fig. 13q), NRL (Fig. 13n), SACLAY (Fig. 13r), have a smaller spread compared to the observations (Fig. 5). The remaining models, particularly LAMONT (Fig. 13l), HAWAII (Fig. 13j), and UKMO (Fig. 13x) have realistic spread although LAMONT (Fig. 13l) has a tendency towards bimodality. Many of the distributions are close to the normal distribution (dashed line) with the exception of a few models.
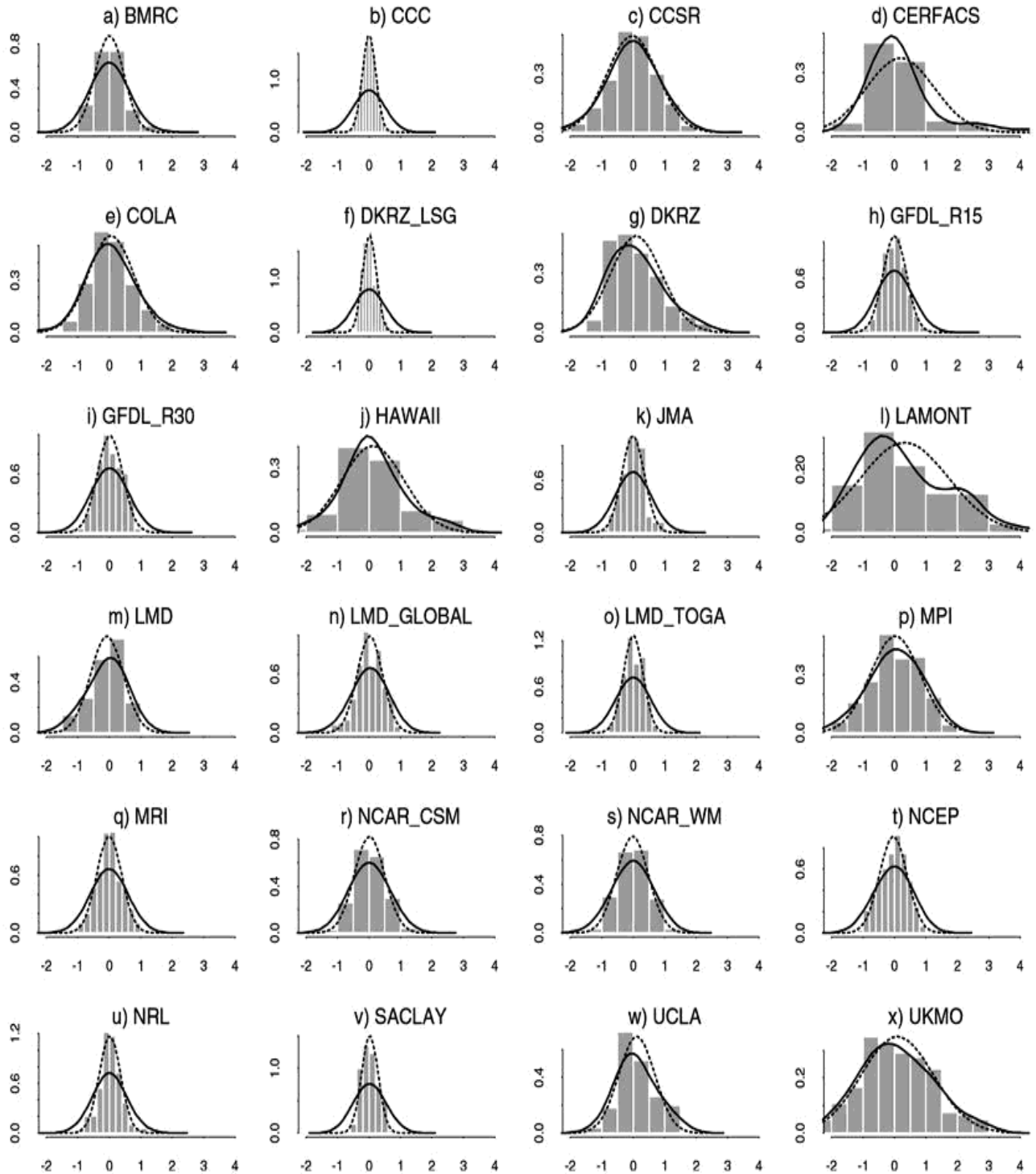
Fig. 13. Histograms (*bars*) and probability distribution functions of the different Niño-3 indices (*solid*). The normal distributions having the same means and variances as the corresponding times series are also shown (*dotted*). Note that because of the wide range of variance in the different indices, the scales of the vertical axes are not identical. The abscissa is the Niño-3 index (°C)

Figure 14 shows the plot of the quantiles of the different Niño-3 indices versus the quantiles of the standard Normal. The same plot for the observed Niño-3 index is also shown for comparison. Unlike the observations, many models are normally distributed with a linear transfer function. The curves in Fig. 14 show significant differences compared to the observations. Some models are positively skewed (Fig. 14d, g, j, u) in agreement with the observations whereas few others show negative skewness (Fig. 14c, e, m, n). Using the Kolmogorov-Smirnov statistic to test the null hypothesis of normality, i.e. linearity, versus non-normality, we find that at 99% confidence level 13 models out of 24 are normal. In the remaining 11 models, seven are clearly nonlinear (Fig. 14c, d, f, g, l, u, w) whereas the other four do not show obvious nonlinearity (Fig. 14h, j, m, t), see the last column of Table 4 for the *P*-values. Moments and robust measures of skewness and kurtosis of the different Niño-3 indices are also shown in Table 4 (columns 4 to 8).
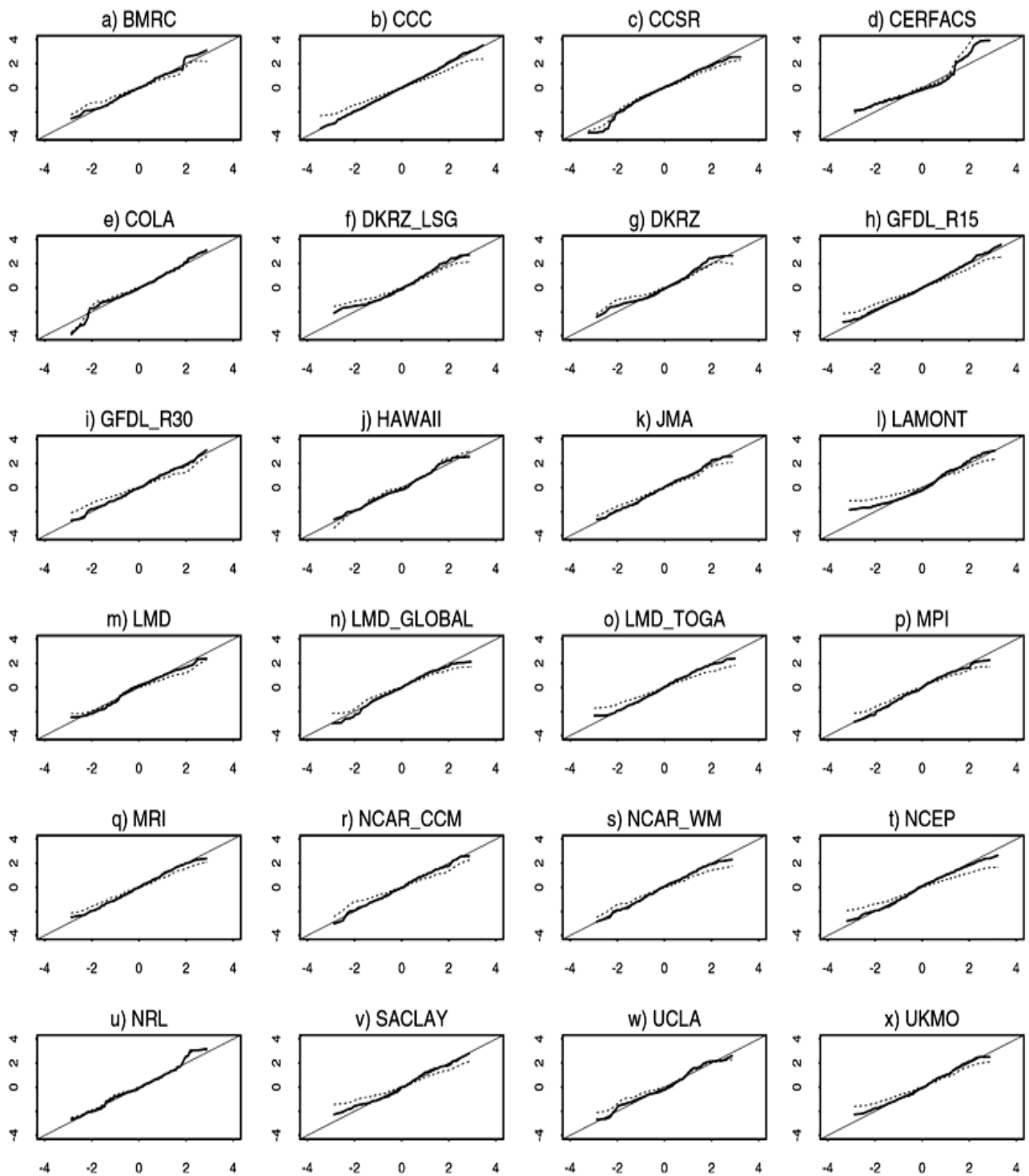
Fig. 14. The quantiles of the standardised Niño-3 indices versus the quantiles of the standard normal (*bold*). The *dotted line* is for the observed Niño-3 index. The curve expected from the standard normal distribution is shown by the *first diagonal*

Furthermore, the nonlinearity in the most non-normal models is not entirely comparable to that seen in the observations. For example, the non-normal behaviour in the LAMONT model (Fig. 14l) is primarily due to a thinner (than the normal) negative tail rather than a fatter positive tail as found in

the observations (Fig. 12l). A careful examination of Fig. 12l reveals that this is due to the overly long persistence of the negative anomalies. On the other hand the skewness in the CERFACS model (Fig. 14d) is mainly due to the presence of large positive anomalies at the beginning of the record. It is also more leptokurtic than the observations. Moreover, CCSR (Fig. 14c), for example, shows negative skewness, unlike the observations, whereas DKRZ-LSG (Fig. 14f) and LAMONT (Fig. 14l) are more platykurtic than observations (Table 4).

4.4

Relation between moments

Neelin (*1991*), and Li (*1997*) have suggested that El Niño variance strongly depends on the background mean state of the atmosphere and the ocean and particularly on the zonal mean thermocline depth in the equatorial Pacific. Meehl et al. (*2001*) found that the vertical mixing (background vertical diffusivity parameter) is an important factor in contributing to the thermocline intensity (defined as the depth range between the 16 °C and 22 °C isotherms at 155°W) and hence acting on the variability of El Niño.

We have addressed this question by looking at the relationship between the means and the spread of the different Niño-3 SST time series. Figure 15a shows a plot of the first L-moment, L_1, versus the second L-moment, L_2 for all Niño-3 indices. The observed value is shown as open circle. The dotted line (Fig. 15a) shows the linear regression fit between L_2 and L_1, $L_2 = 0.044 L_1 - 0.796$. The F-statistic of this model is 2.365 with 1 and 22 degrees of freedom and a *P*-value of 0.138 (with R^2 = 0.097). The regression model shows that the slope of the regression line is not significantly different from zero and, therefore, unlike Mechoso et al. (*1995*), no evidence exists for a significant association between ENSO variance and the background mean state. The few outer models that contribute to the regression are shown in Fig. 15a. This study suggests, unlike Neelin (*1991*) and Li (*1997*), that El Niño variance does not particularly depend on the background mean state. We have also investigated the relationship between the spread of the Niño-3 indices (L_2) and the L-moment ratio measure of skewness (τ_3) in the different models. No evidence for such a relationship is found. The *P*-value for the regression fit is 0.058. Furthermore, the top five most positively skewed models (CERFACS, LAMONT, DKRZ, UCLA, DKRZ-LSG) do not correspond to the models having the five highest spreads (LAMONT, UKMO, HAWAII, CERFACS, DKRZ).
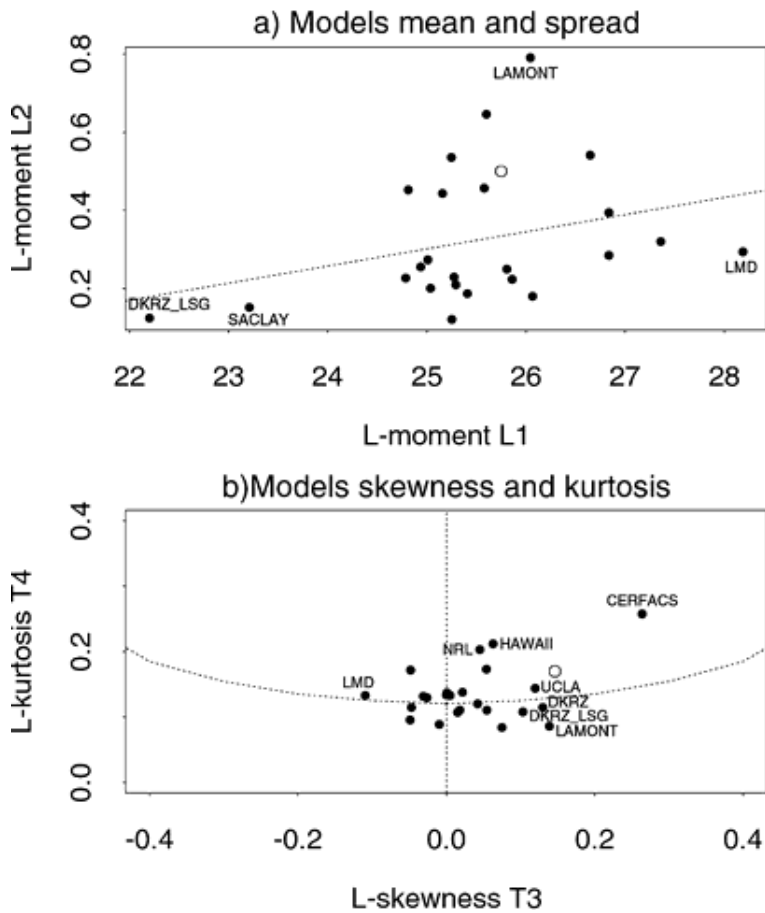
Fig. 15. a Scatter plot of the different models Niño-3 SST means (L_1) versus the L-moment estimate of the spread (L_2). The *dotted line* shows a linear regression fit. Models outside the main cluster are identified. The observed values are shown as an open circle. **b** Scatter plot between the L-moment ratio measures of skewness (τ_3) and kurtosis (τ_4). The *dotted line* shows the relationship for the gamma distribution. The crossing between *this curve* and the *vertical line* corresponds to the values for the normal distribution. The observed values are also shown as an *open circle*. The most non-normal models at 99% confidence are also shown

---

Figure 15b shows a plot of the L-moment ratio measure of skewness (τ_3) versus the L-moment ratio measure of kurtosis (τ_4). The corresponding values for the observations are shown as open circle while the dotted curve indicates the relationship for the gamma distribution. The crossing between this curve and the vertical line (zero-skewness) indicates the values for the normal distribution. Note that most models tend to cluster around the normal distribution. The most non-normal models at the 99% confidence are also shown (Fig. 15b).

5

Conclusions

Novel and robust techniques have been introduced and used to estimate the nonlinear transfer function for Niño-3 sea surface temperature. These techniques are based on probability and

cumulative distribution functions, quantile-quantile plots, boxplots, and L-moments. A simple nonlinear stochastic model is developed for the Niño-3 sea surface temperature time series. The model is based on the observed nonlinear transfer function between the quantiles of the Niño-3 index and the quantiles of the thermocline depth anomalies, which explains the resulting changes in SST as a response to changes in thermocline depth.

The robust techniques confirm that observed Niño-3 sea surface temperature anomalies are significantly non-normal due to the presence of positive skewness. The estimated transfer function shows that observed Niño-3 SSTs saturate only at deep thermocline depths. When the thermocline is shallow, the SST is linearly related to the depth anomalies of the thermocline in the Niño-3 region due to active mixing processes. These results contradict the saturation at shallow thermocline depth assumed by Zebiak and Cane (1987) and Battisti (*1988*). The observed annual cycle shows inhomogeneities across the months of the year with most interannual spread in November and December. Positive skewness is most evident in the autumn/winter months.

The majority of the 24 coupled models in ENSIP underestimate the nonlinearity noted in the transfer function of the observed Niño-3 index. Thirteen out of the 24 models gave Niño-3 indices that were normally distributed at 99% confidence. Of the remaining non-normal models only 2 models capture the observed skewness noted in the observation for large SST anomalies. The most non-normal models did not correctly simulate the interannual spread although the phase of the annual cycle was reasonably well simulated. The influence of the background mean state on the interannual spread of Niño-3 sea surface temperature has also been investigated using robust techniques. There is little evidence of a significant relationship between the mean state and the interannual spread of the Niño-3 SST anomalies from different models.

In summary, this study confirms the nonlinearity and the significant departure from normality found in observed Niño-3 SST anomalies (Burgers and Stephenson *1999*; Sardeshmukh et al. *2000*). However, coupled models fail to capture correctly this nonlinearity. There are several possible explanations for this discrepancy. The thermocline depth in the coupled models is perhaps either deeper or shallower than in reality. Alternatively, the background vertical diffusivity may play an important role in ENSO SST variability (Meehl et al. *2001*). Meehl et al. (*2001*) showed that the smaller values of the vertical diffusivity parameter gave larger ENSO variance due to the existence of a sharper thermocline. It would be interesting also to see how this parameter influences nonlinearity in sea surface temperatures.

Appendix 1

L-moments of a random variable

Techniques based on standard moment estimates have long been used. These estimates tend, however, to be robust only for normally distributed data. When the data are not normal those estimates tend to be unsatisfactory and can be sometime biased. For instance if the data contain few outliers then higher order moments will be heavily weighted by those few observations. An alternative approach is the L-moments. These are based on *linear* combination of order statistics hence the name L-statistics.

For a real finite-mean random variable Y with c.d.f. $F(y)$ and quantile function $y_p = F^{-1}(p)$ let $Y_{1:n} \leq Y_{2:n} ... \leq Y_{n:n}$ be the order statistics of a random sample of size n drawn from the distribution F of Y. The L-moments, λ_r, of Y are defined as linear combinations of the expected order statistics:

$$\lambda_r = \frac{1}{r} \sum_{k=0}^{r-1} (-1)^k \binom{r-1}{k} EY_{r-k:r}, \quad r = 1, 2, \ldots \tag{9}$$

where the notation $EY_{j:r}$ stands for the expectation of the order statistic $Y_{j:r}$, which is given by:

$$EY_{j:r} = \frac{r!}{(j-1)!(r-j)!} \int y (F(y))^{j-1} (1 - F(y))^{r-j} dF(y) . \tag{10}$$

Combining and using simple algebra, λ_r can be expressed in terms of the quantile function y_p as follows,

$$\lambda_r = \int_0^1 F^{-1}(p) P_{r-1}^*(p) dp = \int_0^1 y_p P_{r-1}^*(p) dp \tag{11}$$

where P_r^* is the r'th shifted Legendre polynomial, $P_r^*(u) = P_r(2u - 1)$, which is given by

$$P_r^*(u) = \sum_{k=0}^{r} (-1)^{r-k} \binom{r}{k} \binom{r+k}{k} u^k . \tag{12}$$

For example the first four L-moments are given by

$$\lambda_1 = EY,$$

$$\lambda_2 = \frac{1}{2} E(Y_{2:2} - Y_{1:2}) = \int_0^1 y_p (2p - 1) dp,$$

$$\lambda_3 = \frac{1}{3} E(Y_{3:3} - 2Y_{2:3} + Y_{1:3}) = \int_0^1 y_p (6p^2 - 6p + 1) dp, \tag{13}$$

$$\lambda_4 = \frac{1}{4} E(Y_{4:4} - 3Y_{3:4} + 3Y_{2:4} - Y_{1:4}) = \int_0^1 y_p (20p^3 - 30p^2 + 12p - 1) dp$$

and they represent respectively the mean, and measures of spread, skewness, and kurtosis. Any distribution with finite mean is uniquely specified by its L-moments even if some of its conventional moments do not exist (see Hosking *1990* for details). The L-moments can be standardised by λ_2 to yield the L-moment ratios τ_r (Eq. 8). The sample estimate of λ_r can be obtained by linear combination of the ordered data values using Eqs. (11) and (12) (see Hosking *1990* for details). Note that because the shifted Legendre polynomials are orthogonal on the interval (0, 1), Eq. (11) can be "inverted" to yield the expansion of the quantile function in terms of the L-moments (Eq. 6).

References

AchutaRao K, Sperber KR, and the CMIP modelling Groups (2002) The El Niño Southern Oscillation in coupled GCMs. Clim Dyn (in press)

Battisti DS (1988) Dynamics and thermodynamics of a warming event in a coupled tropical atmosphere-ocean model. J Atmos Sci 45: 2889-2919

Battisti DS, Hirst AC (1989) Interannual variability in a tropical atmosphere-ocean model: influence of the basic state, ocean geometry and nonlinearity. J Atmos Sci 46: 1687-1712

Bjerknes J (1969) Atmospheric teleconnections from the equatorial Pacific. Mon Weather Rev 97: 163-172

Bjerknes J (1972) Large-scale atmospheric response to the 1964-65 Pacific equatorial warming. J Phys Oceanogr 2: 212-217

Burgers G (1999) The El Niño stochastic oscillator. Clim Dyn 15: 521-531

Burgers G, Stephenson DB (1999) The "Normality" of El Niño. Geophys Res Lett 26: 1027-1030

Cane MA, Zebiak SE (1985) A theory for El Niño Southern Oscillation. Science 228: 1085-1087

Davey MK, Huddleston M, Sperber KR (2001) STOIC: A study of coupled GCM climatology and variability in tropical ocean regions. CLIVAR-WGSIP STOIC project report

Graham NE, White WB (1988) The El Niño cycle: a natural oscillator of the Pacific ocean-atmosphere system. Science 240: 1293-1302

Hannachi A (2001) Toward a nonlinear identification of the atmospheric response to ENSO. J Clim 14: 2138-2149

Hoerling MP, Kumar A, Zhong M (1997) EL-Nino, LA Nina, and the nonlinearity of their teleconnections. J Clim 10: 1769-1786

Horel JD, Wallace JM (1981) Planetary-scale atmospheric phenomena associated with the Southern Oscillation. Mon Weather Rev 109: 813-829

Hosking JRM (1990) L-moments: analysis and estimation of distributions using linear combinations of order statistics. J R Statist Soc B 52: 105-124

Hoskins BJ, Karoly DJ (1981) The steady linear response of a spherical atmosphere to thermal and orographic forcing. J Atmos Sci 38: 1179-1196

Jin FF (1997) An equatorial ocean recharge paradigm for ENSO. Part I: conceptual model. J Atmos Sci 54: 811-829

Jin FF, Neelin JD, Ghil M (1994) El Niño on the Devil's staircase: annual subharmonic steps to chaos. Science 264: 70-72

Kindle JC, Phoebus PA (1995) The ocean response to operational westerly wind bursts during the 1991-1992 El Niño. J Geophys Res 100: 4893-4920

Kleeman R (1993) On the dependence of the hindcast skill on ocean thermodynamics in a coupled ocean-atmosphere model. J Clim 6: 2012-2033

Lau N-C, Philander SGH, Nath MJ (1992) Simulation of ENSO-like phenomena with a low-resolution coupled GCM of the global ocean and atmosphere. J Clim 5: 284-307

Latif M et al (2002) ENSIP: the El Niño simulation intercomparison project. Clim Dyn 18: 255-276

Lazante JR (1996) Resistant, robust and non-parametric techniques for the analysis of climate data: theory and examples, including applications to historical radiosonde station data. Int J Climatol 16: 1197-1226

Li T (1997) On the phase transition of the El Niño-Southern Oscillation: a stationary SST mode. J Atmos Sci 54: 2872-2887

Mardia KV (1980) Tests of univariate and multivariate normality. In: Krishnaiah PR (ed) Handbook of statistics 1: analysis of variance, North Holland, pp 279-320

McGill R, Tukey JW, Larsen WA (1978) Variations of boxplots. The Am Statistician 32: 12-16

McPhaden MJ and 14 co-authors (1998) The Tropical Ocean-Global Atmosphere (TOGA) observing system: A decade of progress. J Geophys Res 103: 14,169-14,240

Mechoso CR et al (1995) The seasonal cycle over the tropical Pacific in general circulation models. Mon Weather Rev 123: 2825-2838

Meehl GA, Boar JG, Covey C, Latif M, Stouffer RJ (2000) The Coupled Model Intercomparison Project (CMIP). Bull Am Meteorol Soc 81: 313-318

Meehl GA, Gent PR, Arblaster JM, Otto-Bliesner BL, Brady EC, Craig A (2001) Factors that affect the amplitude of El Nino in global coupled climate models. Clim Dyn 17: 515-526

Munnich M, Cane MA, Zebiak SE (1991) A study of self-excited oscillations of the tropical ocean-atmosphere system. Part II: nonlinear cases. J Atmos Sci 48: 1238-1248

Neelin JD (1990) A hybrid coupled general circulation model for El Niño studies. J Atmos Sci 47: 674-693

Neelin JD (1991) The slow sea surface temperature model and the fast wave limit: analytic theory

for tropical interannual oscillation and experiments in a hybrid coupled model. J Atmos Sci 48: 584-606

Neelin JD, Battisti DS, Hirst AC, Jin FF, Wakata Y, Yamagata T, Zebiak S (1998) ENSO theory. J Geophys Res 103: 14,261-14,290

Penland C, Magorian T (1993) Prediction of Niño-3 sea surface temperatures using linear inverse modelling. J Clim 6: 1067-1076

Penland C, Sardeshmukh P (1995a) The optimal growth of tropical sea surface temperature anomalies. J Clim 8: 1999-2024

Penland C, Sardeshmukh P (1995b) Error and sensitivity analysis of geophysical eigen-systems. J Clim 8: 1988-1998

Philander SGH (1990) El Niño, La Niña, and the Southern Oscillation. Academic Press, New York

Rayner MA, Horton EB, Parker DE, Folland CK, Hackett RB (1996) Version 2.2 of the global sea-ice and sea-surface temperature data set, 1903-1994. Hadley Centre Technical Note 74. Hadley Centre for Climate Prediction, Bracknell, UK

Reynolds RW, Smith TM (1994) Improved global sea surface temperature analysis. J Clim 7: 929-948

Salstein DA, Rosen RD (1984) El Niño and the earth's rotation. Oceanus 27: 52-57

Sardeshmukh PD, Compo GP, Penland C (2000) Changes of probability associated with El Niño. J Clim 13: 4268-4286

Silverman BW (1994) Density estimation for statistics and data analysis. Chapman and Hall, London

Sperber KR, Hameed S, Gates WL, Potter GL (1987) Southern oscillation simulated in a global climate model. Nature 329: 140-142

Stone L, Sapirin PI, Hupert A, Price C (1998) El Niño chaos: the role of noise and stochastic resonance on the ENSO cycle. Geophys Res Lett 25: 175-178

Suarez MJ, Schopf PS (1988) A delayed action oscillator for ENSO. J Atmos Sci 45: 3283-3287

Tett S (1995) Simulation of El Niño/Southern Oscillation-like variability in a global AOGCM and its response to CO_2 increase. J Clim 8: 1473-1502

Timmermann A, Oberhuber J, Bacher A, Esch M, Latif M, Roeckner E (1999) Increased El Niño frequency in a climate model forced by future greenhouse warming. Nature 398: 694-697

Thompson CJ, Battisti DS (2000) A linear stochastic dynamical model of ENSO. Part I: model development. J Clim 13: 2818-2832

Thompson CJ, Battisti DS (2001) A linear stochastic dynamical model of ENSO. Part II: analysis. J Clim 14: 445-466

Trenberth KE (1997) The definition of El Niño. Bull Am Meteorol Soc 78: 2771-2777

Trenberth KE, Branstator GW, Karoly D, Kumar A, Lau N-C, Ropelewski C (1998) Progress during TOGA in understanding and modelling global teleconnections associated with tropical sea surface temperatures. J Geophys Res 103: 14,291-14,324

Tukey JW (1990) Data-based graphics: visual display in the decades to come. Statist Sci 5: 327-339

Von Storch H, Zwiers FW (1999) Statistical analysis in climate research. Cambridge University Press, Cambridge

Wolter K, Timlin MS (1998) Measuring the strength of ENSO events: How does 1997/98 rank? Weather 53: 315-324

Wunsch C (1999) The interpretation of short climate records, with comments on the North Atlantic and Southern Oscillations. Bull Am Meteorol Soc 80: 245-255

Xie P, Arkin PA (1996) Analyses of global monthly precipitation using gauge observations, satellite estimates, and numerical model predictions. J Clim 9: 840-858

Zebiah SE, Mark AC (1987) A mode E1 Niño-Southern Oscillation. Mon Weather Rev 115: 2262-2278

Zhang Y, Wallace JM (1996) Is climate variability over the North Pacific a linear response to ENSO? J Clim 9: 1468-1478